Supporting Information

Hollow Black $TiAlO_x$ Nanomposites for Solar Thermal Desalination

Luocai Yi, Dianpeng Qi, Ping Shao, Chaojun Lei, Yang Hou, Pingwei Cai, Genxiang Wang, Xiaodong Chen*, Zhenhai Wen**

Contents

1 Reagents

TiO_2 powder with average particle size of ~ 200 nm and $AlCl_3$ powder (Shanghai Macklin Biochemical Co., Ltd). Poly(vinylidene fluoride) (PVDF) was obtained from Arkema (France). Al powder was obtained from Energy chemical Company. NaCl, $MgCl_2 \cdot 6H_2O$, KCl, $MgSO_4$, $NaHCO_3$, $CaCl_2$, NaBr, and N, N-Dimethylformamide (DMF) was purchased from Sinopharm Chemical Reagent Co., Ltd. All the materials were used as starting materials without further purification.

2. The calculation of solar absorption of samples (TiO_2, $TiAlO_x$-y-H^+ and TA-y-H^+)

The solar absorption of all the samples can be calculated by the equation S1[1]:

$$A=\frac{\int(1-R)\cdot S\cdot d\lambda}{\int S\cdot d\lambda} \quad (1)$$

where A is the solar absorption, R is the reflectance of the sample, S is solar spectral irradiance (W m^{-2} nm^{-1}), λ is the wavelength (nm), the (1-R)·S represents the sample absorption of solar spectral irradiance. Therefore, the solar absorption of samples can be calculated to be presented in Table S1, respectively.

Table S1. Average reflectance of photothermal materials in different spectrum region.

Sample	UV (%) [a)]	Visible (%) [b)]	Infrared (%) [c)]
TiO_2	25.06	97.56	93.54
$TiAlO_x$-100-H^+	24.49	94.09	78.06
$TiAlO_x$-200-H^+	19.65	34.60	15.89
$TiAlO_x$-300-H^+	21.84	24.81	15.25
$TiAlO_x$-400-H^+	13.21	12.17	9.69
$TiAlO_x$-500-H^+	11.44	9.87	11.84
$TiAlO_x$-600-H^+	10.76	9.54	9.93
TA-100-H^+	24.71	92.88	81.93
TA-200-H^+	25.30	92.25	79.80
TA-300-H^+	26.00	87.86	76.39
TA-400-H^+	25.38	84.88	83.10
TA-500-H^+	12.80	10.95	11.83
TA-600-H^+	10.76	9.64	11.13
Pure PVDF	102.35	97.59	89.96
$TiAlO_x$ membrane	11.80	9.67	10.78

[a)]UV light: λ≤400 nm; [b)]visible light: 400<λ≤760 nm; [c)]infrared light: λ≥760 nm.

Table S2. Solar absorption of photothermal materials in different spectrum region.

Sample	Total	UV (%) [a)]	Visible (%) [b)]	Infrared (%) [c)]
Solar	100	7	50	43
TiO_2	9.24	5.25	1.22	2.78
$TiAlO_x$-100-H^+	17.68	5.29	2.96	9.44
$TiAlO_x$-200-H^+	74.49	5.62	32.7	36.17
$TiAlO_x$-300-H^+	79.51	5.47	37.6	36.44
$TiAlO_x$-400-H^+	88.83	6.08	43.92	38.83
$TiAlO_x$-500-H^+	89.17	6.2	45.06	37.91

$TiAlO_x$-600-H^+	90.21	6.25	45.23	38.73
TA-100-H^+	16.6	5.27	3.56	7.77
TA-200-H^+	17.79	5.23	3.87	8.69
TA-300-H^+	21.4	5.18	6.07	10.15
TA-400-H^+	20.05	5.22	7.56	7.27
TA-500-H^+	88.54	6.1	44.52	37.91
TA-600-H^+	89.64	6.25	45.18	38.21
Pure PVDF	5.36	-0.16	1.21	4.32
$TiAlO_x$ membrane	89.70	6.17	45.17	38.36

[a)]UV light: $\lambda \leq 400$ nm; [b)]visible light: $400 < \lambda \leq 760$ nm; [c)]infrared light: $\lambda \geq 760$ nm.

3. XRD patterns, digital images, SEM images HRTEM images, elemental abundances, XPS, BET, and UV-Vis-NIR diffuse reflectance spectra of products

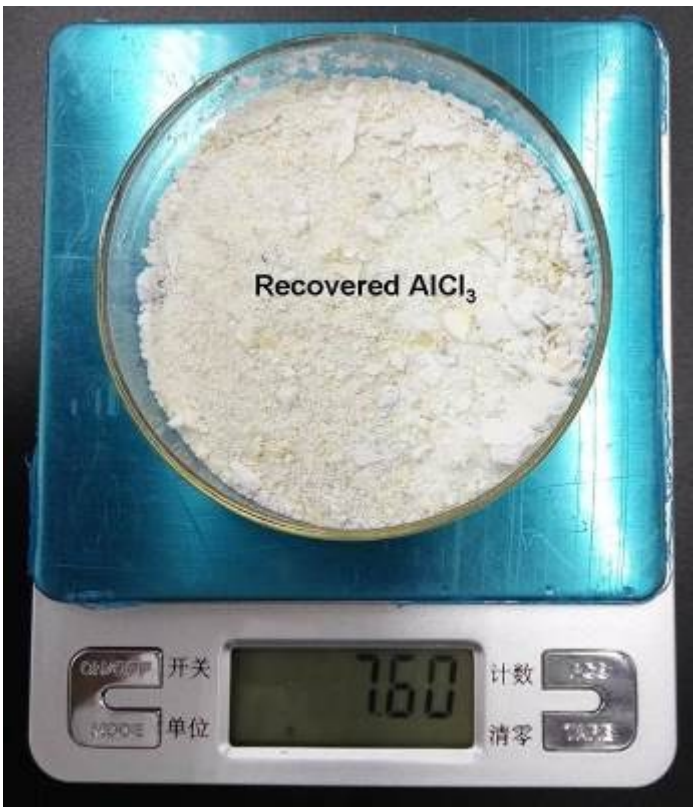

Figure S1. Digital photos of the recycled $AlCl_3$.

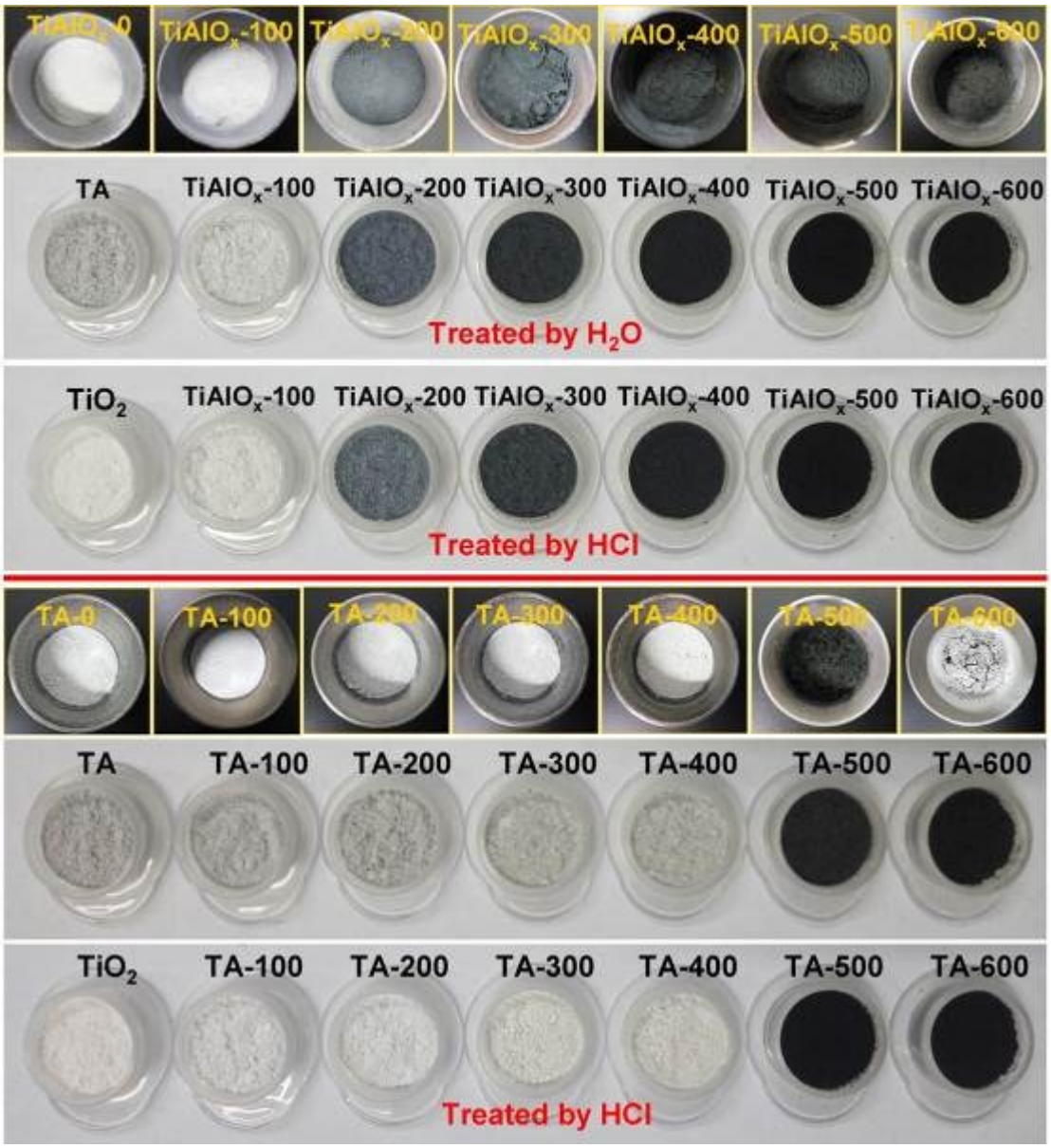

Figure S2. Digital photos of the $TiAlO_x$-y, $TiAlO_x$-y-H_2O, $TiAlO_x$-y-H^+, TA-y, and TA-y-H^+, respectively.

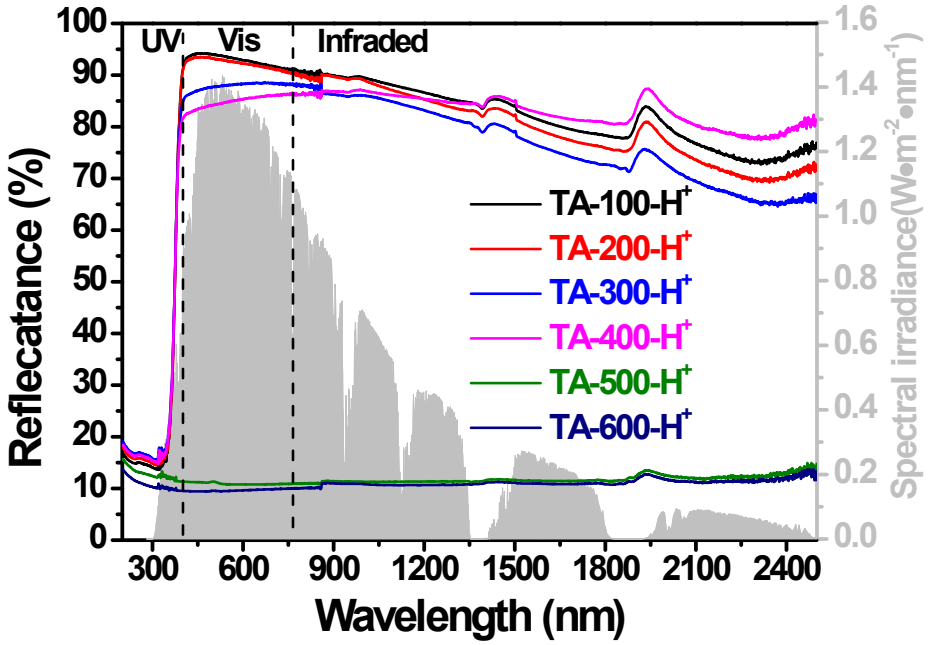

Figure S3.UV-Vis-NIR diffuse reflectance spectra of TA-y-H^+.

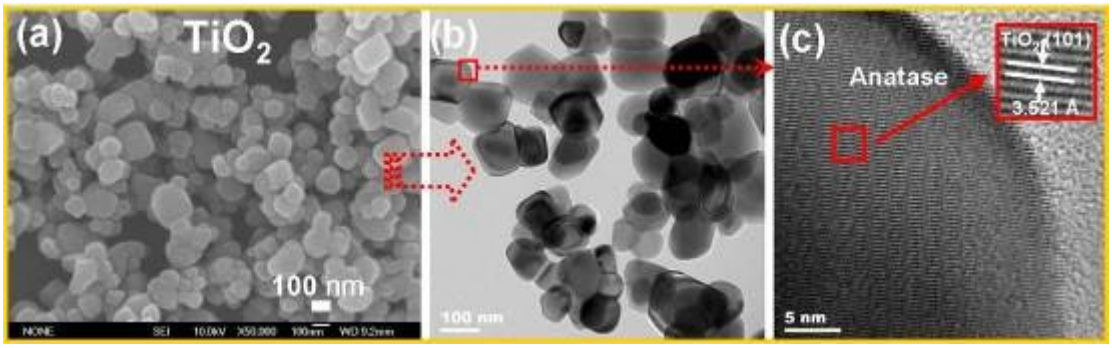

Figure S4. (a-c) SEM, TEM, and HRTEM images of commercial TiO_2 powder, respectively.

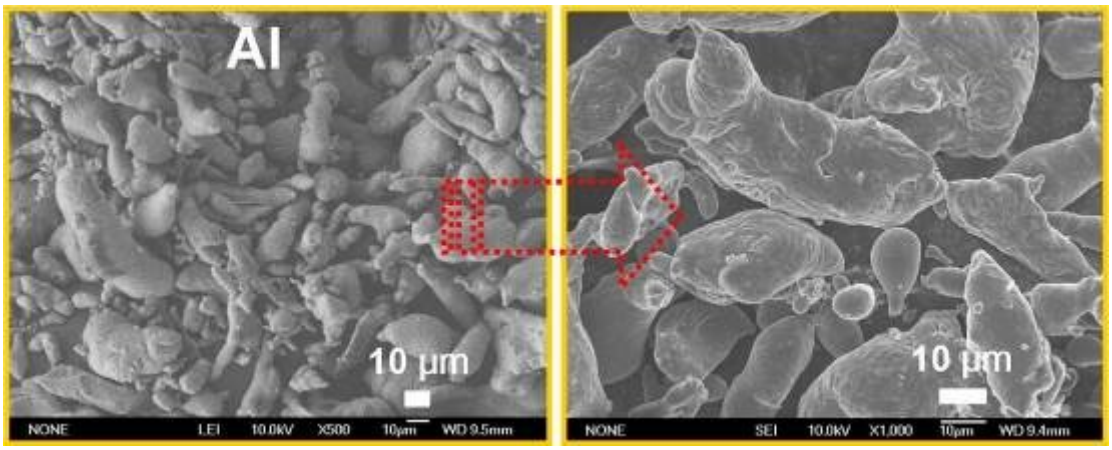

Figure S5. SEM images of commercial Al powder.

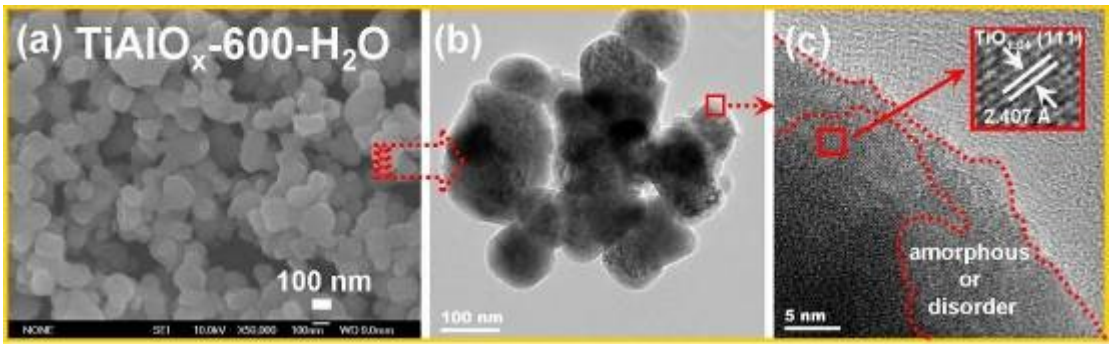

Figure S6. (a-c) SEM, TEM, HRTEM images of TiAlO$_x$-600-H$_2$O, respectively.

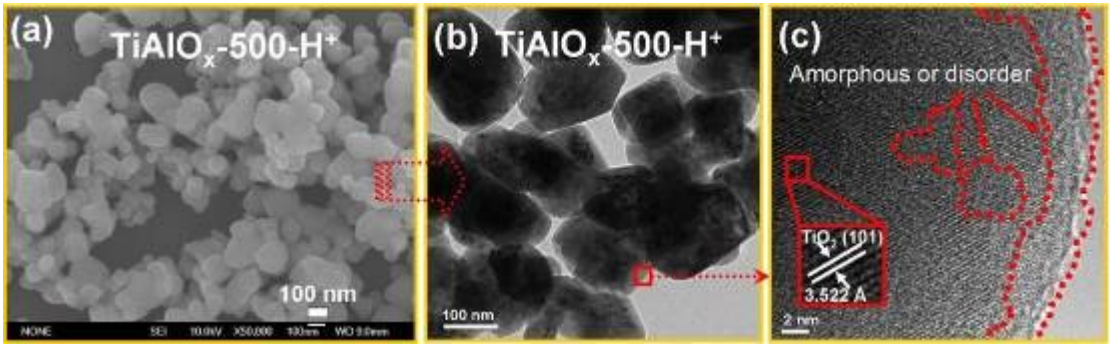

Figure S7. (a-c) SEM, TEM, and HRTEM images of $TiAlO_x$-500-H^+ respectively.

Table S3. Measured concentration of four primary elements, Ti, Al, and O in an hollow black $TiAlO_x$-600-H^+ by ICP-OES.

Element	Ti	Al[a)]	O
Weight %	61.68%	29.56%	8.76%
Atomic %	43.88%	37.41%	18.71%
	Ti : Al = 1.29 : 1.10		

[a)] In the process of testing, a small amount of white powder is not dissolved in acid (Hydrofluoric acid and aqua regia), which may result in low aluminum content.

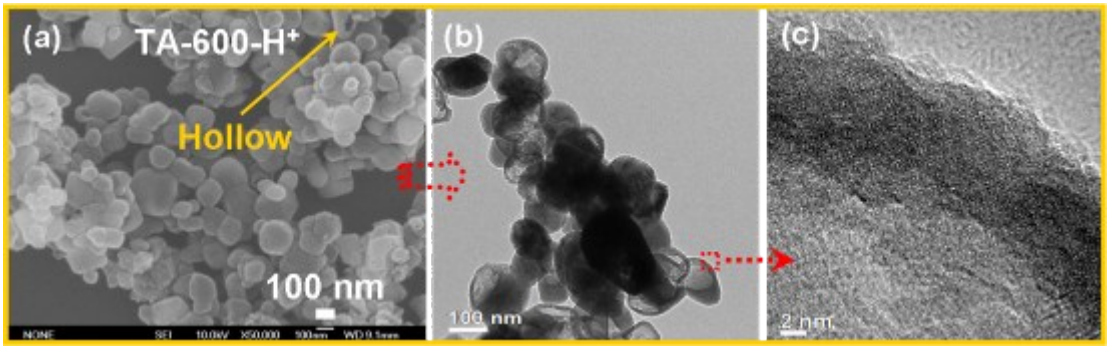

Figure S8. (a-c) SEM, TEM, and HRTEM images of TA-600-H^+, respectively

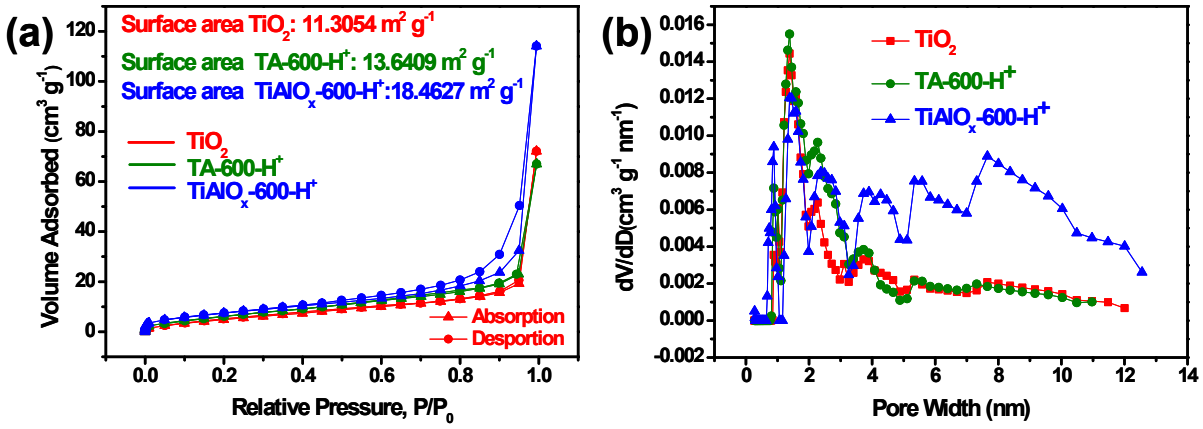

Figure S9. N_2 adsorption-desorption isotherm (a) and pore size distribution (b) curves of the TiO_2, TA-600-H^+, and $TiAlO_x$-600-H^+.

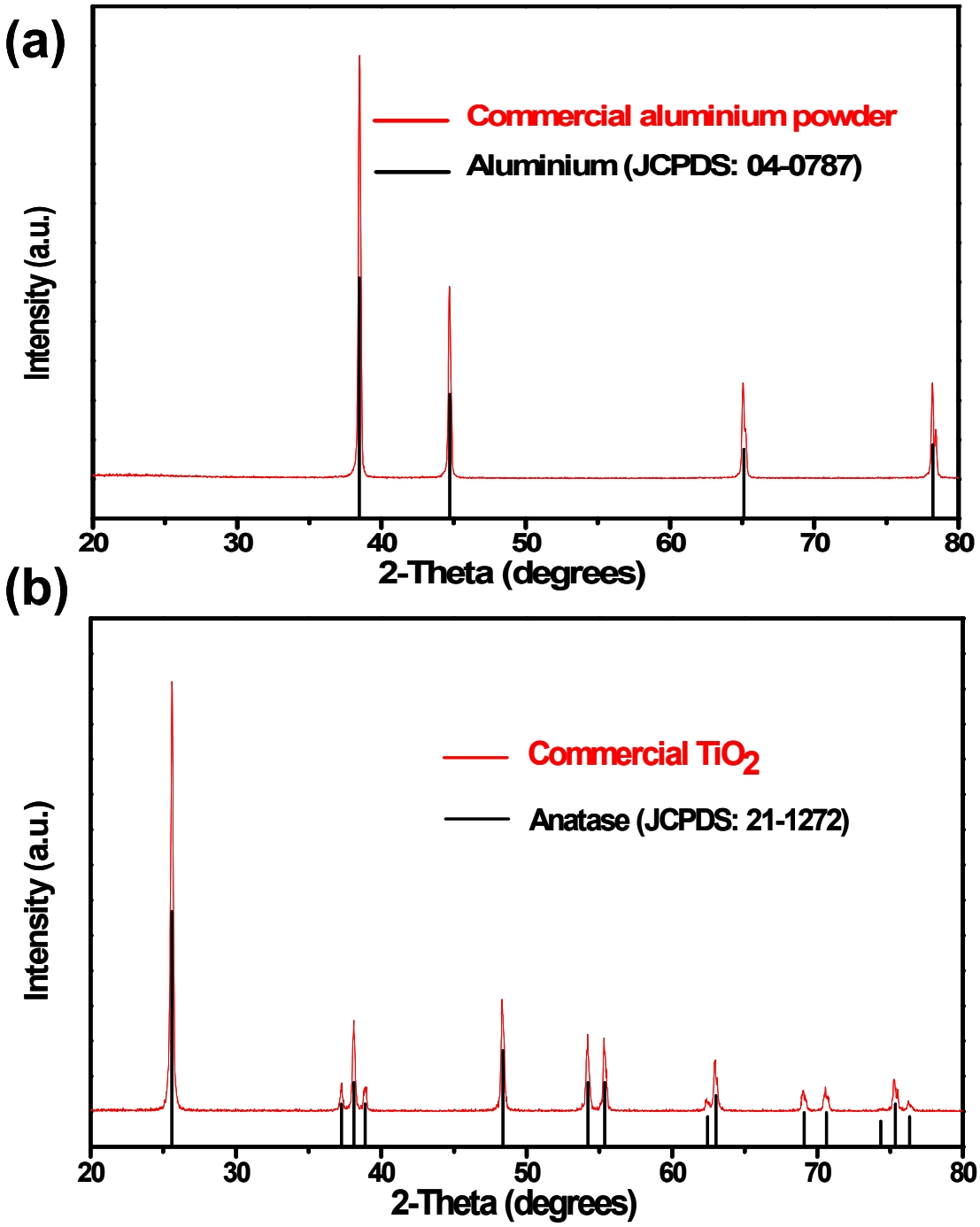

Figure S10. PXRD patterns of (a) commercial Al powder, and (b) commercial TiO_2 powder.

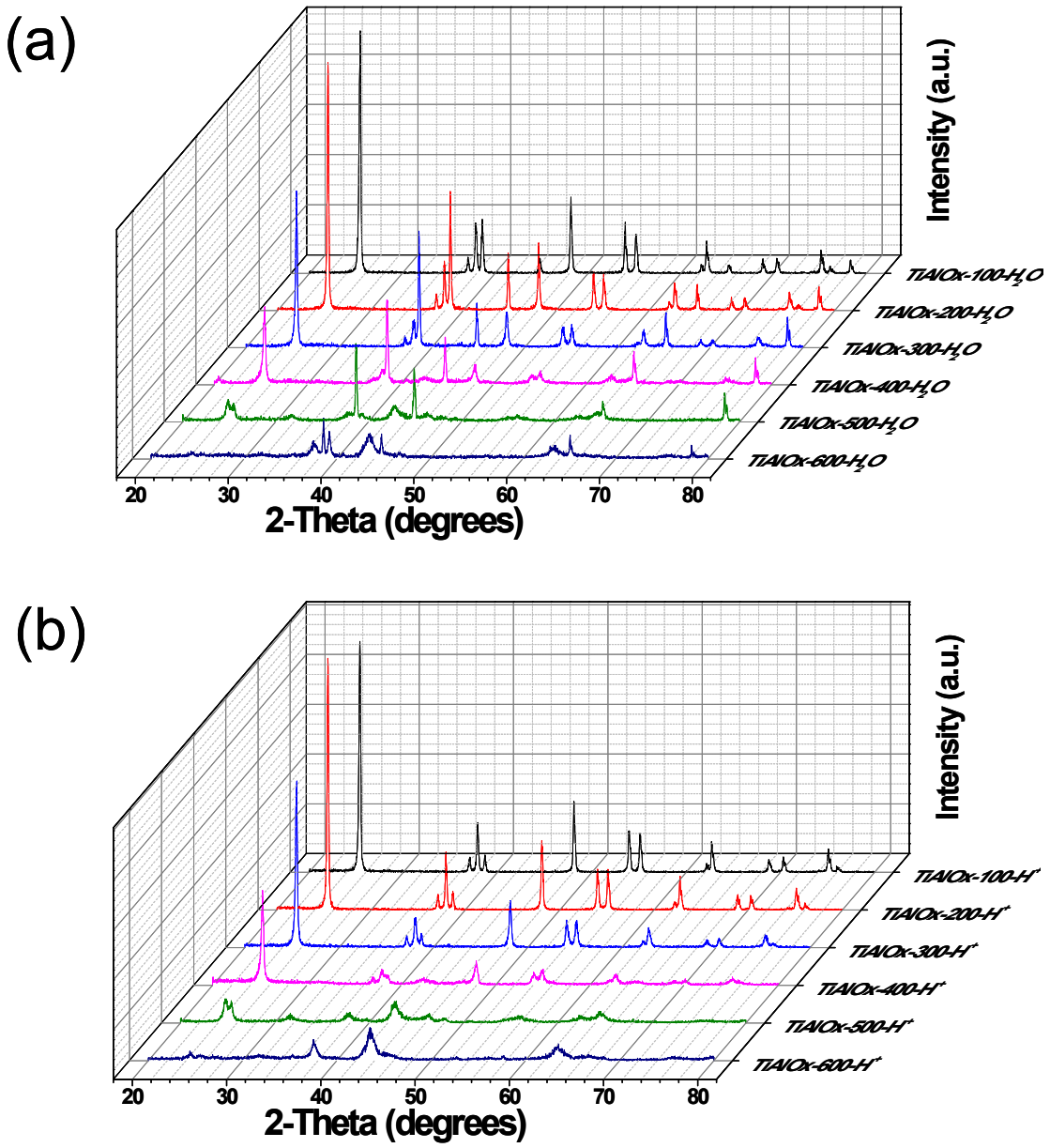

Figure S11. PXRD patterns of (a) $TiAlO_x$-y-H_2O, (b) $TiAlO_x$-y-H^+.

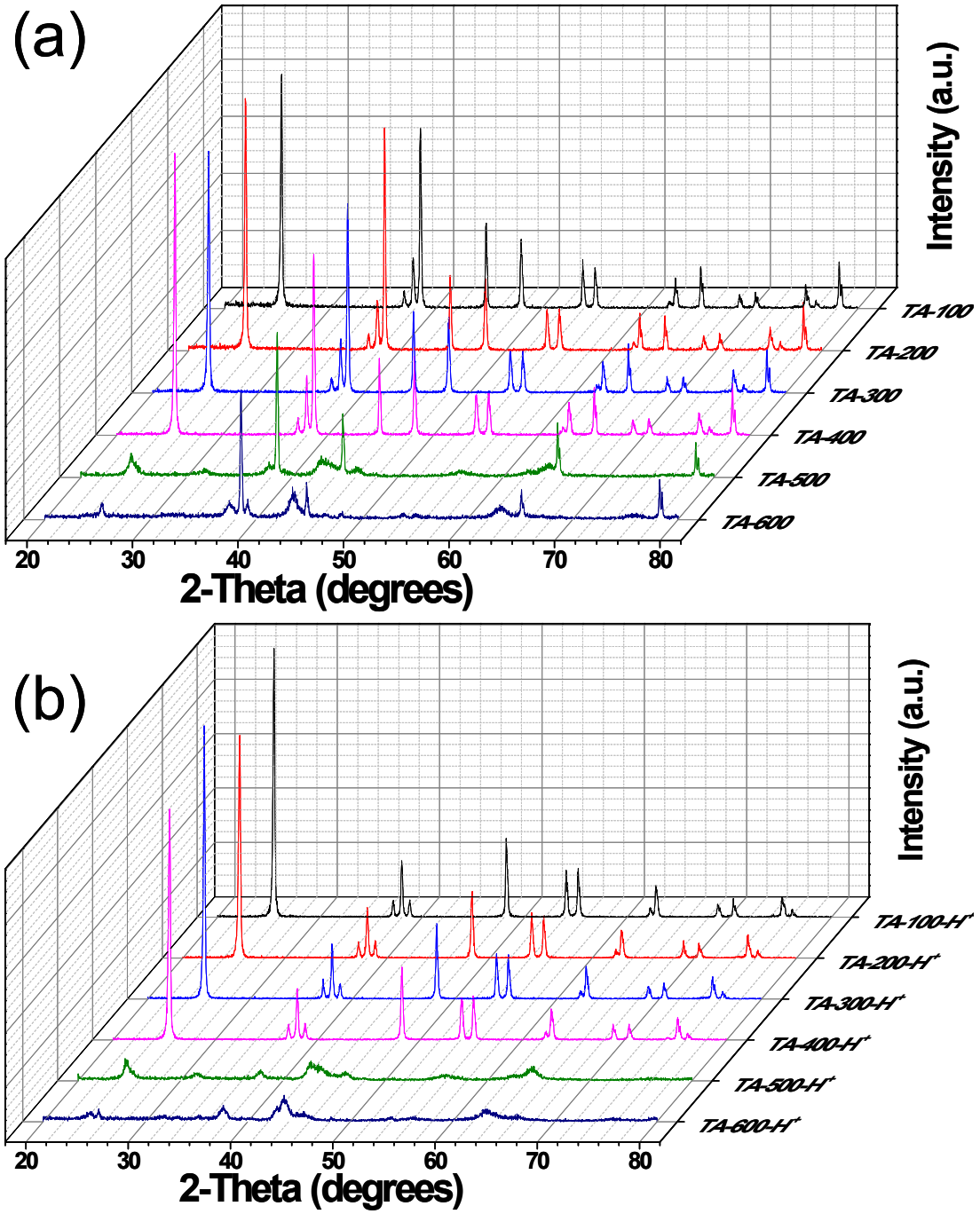

Figure S12. PXRD patterns of (a) TA-y, (b) TA-y-H^+.

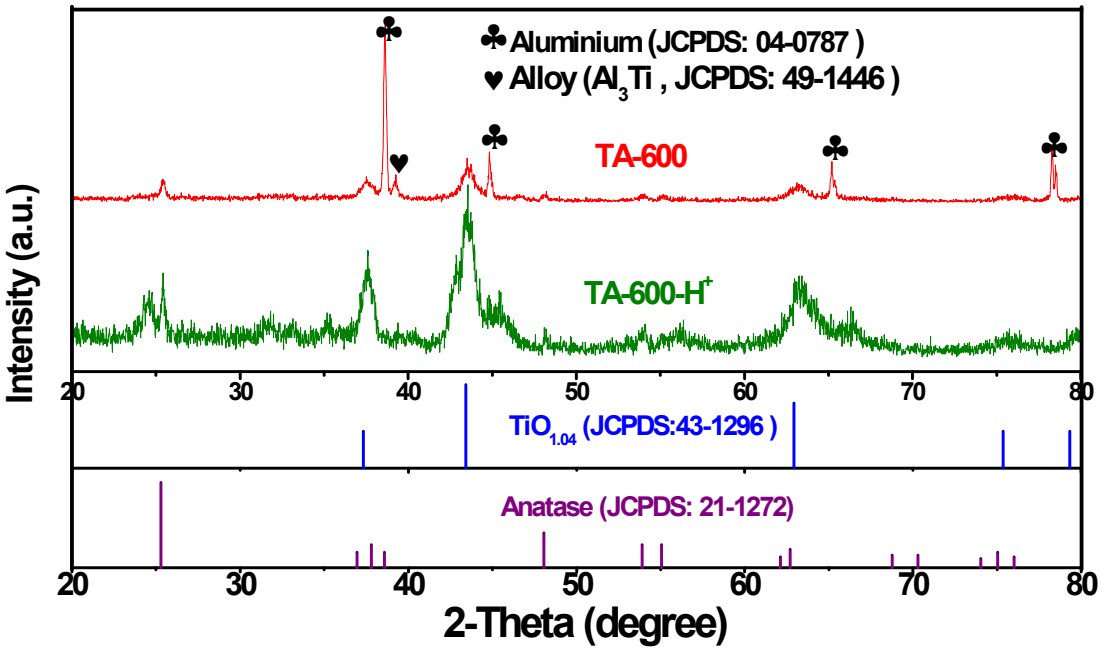

Figure S13. PXRD patterns of (a) TA-600, (b) TA-600-H^+.

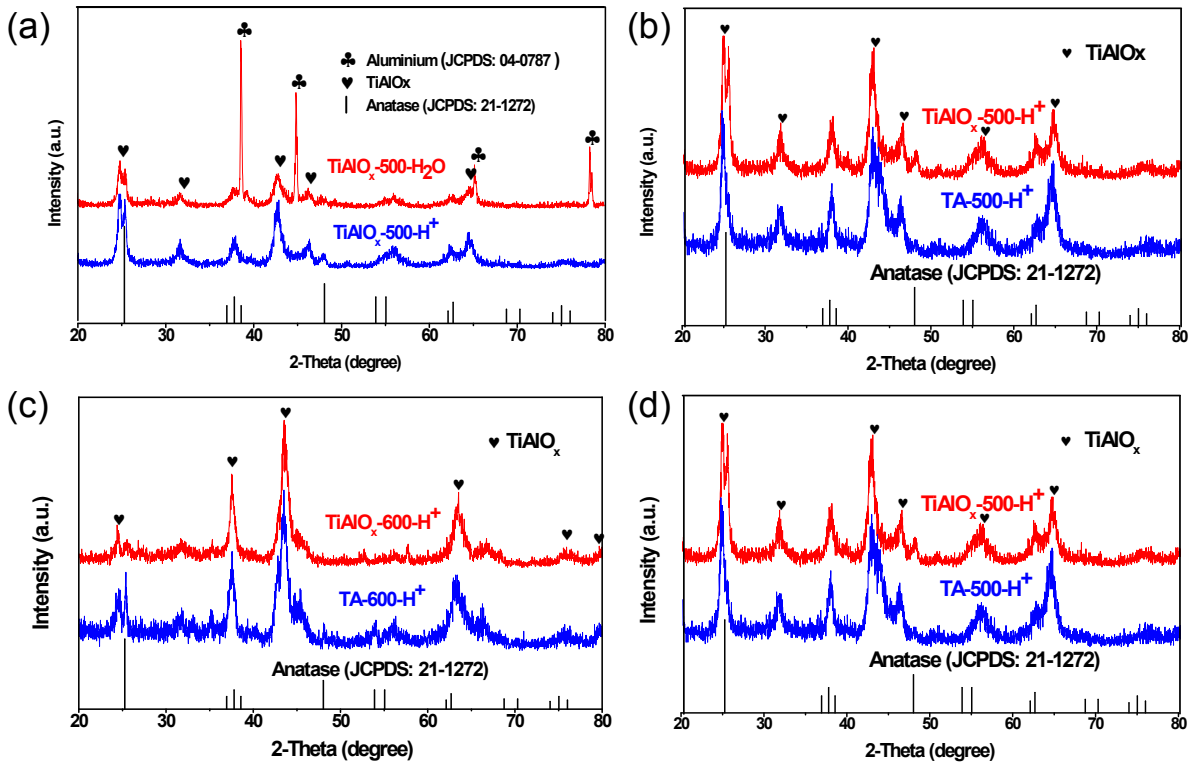

Figure S14. PXRD patterns of (a) $TiAlO_x$-500-H_2O and $TiAlO_x$-500-H^+. (b) $TiAlO_x$-500-H^+ and TA-500-H^+. (c) $TiAlO_x$-600-H^+ and TA-600-H^+. (d) $TiAlO_x$-500-H^+ and TA-500-H^+.

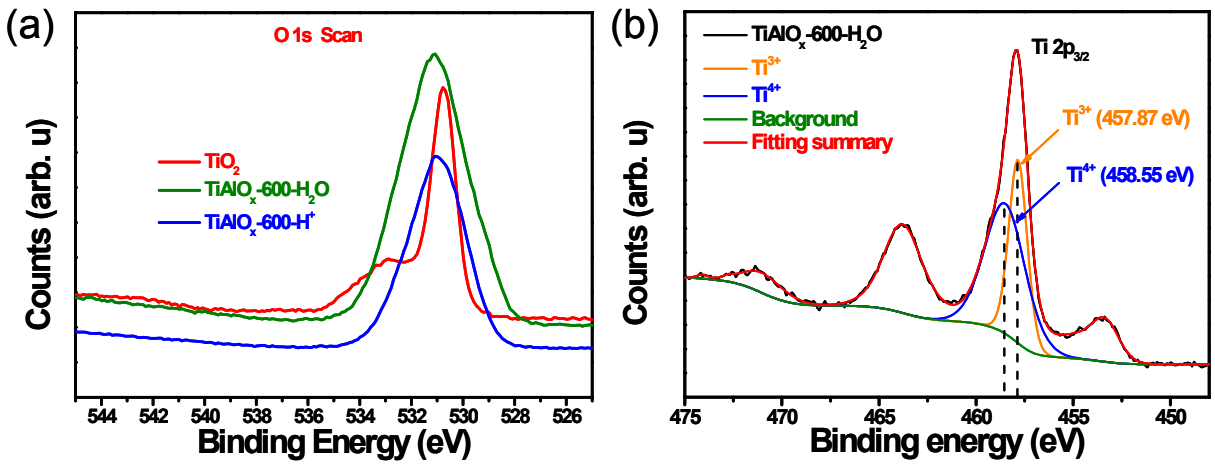

Figure S15. High-resolution XPS spectra for (a) O 1s in TiO_2, $TiAlO_x$-600-H_2O, and $TiAlO_x$-600-H^+. (b) Ti 2p in $TiAlO_x$-600-H_2O.

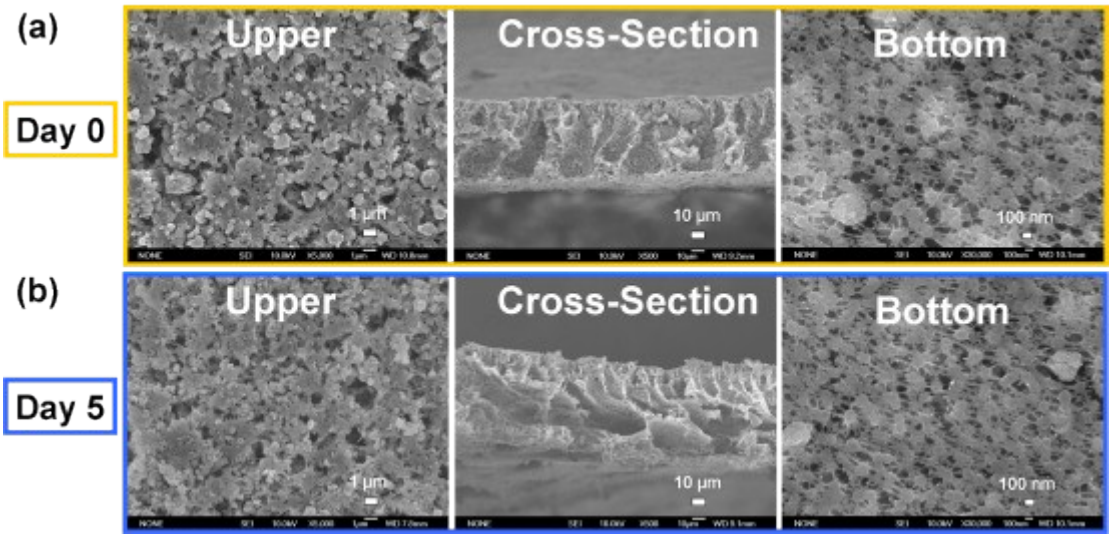

Figure S16. SEM images for the hollow black $TiAlO_x$ membrane in upper surface, cross-section, and bottom surface. One can observe that there is no obvious change in morphology and structure for the membrane (porosity, pore size) during the desalination test for up to 5 days. The results show that the $TiAlO_x$ photothermal membrane has relatively stable desalination performance under long time brine environment.

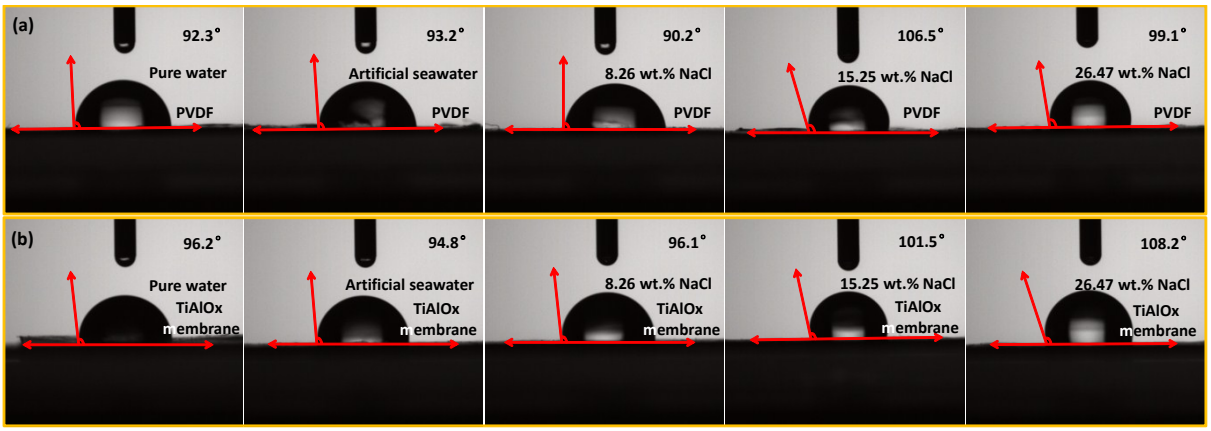

Figure S17. Solution (pure water, artificial seawater, 8.26 wt.% NaCl, 15.25 wt.% NaCl, 26.47 wt.% NaCl) contact angles of (a) PVDF, (b) $TiAlO_x$ membrane. It can be seen that the contact angles of PVDF and $TiAlO_x$ membrane in different solutions are greater than 90°, which indicates that both PVDF and $TiAlO_x$ membrane have non-wetting properties. At the same time, the hydrophobicity of the $TiAlO_x$ membrane increases with the increase of salt concentration, i.e. the contact angles in pure water, artificial seawater, 8.26 wt.% NaCl, 15.25 wt.% NaCl, 26.47 wt.% NaCl are 96.2°, 94.8°, 96.1°, 101.5°, 108.2°, respectively. Moreover, brine with higher salinity is more conducive to membrane floating. It is such non-wetting and light properties that enable the photothermal membrane to float on the water surface.

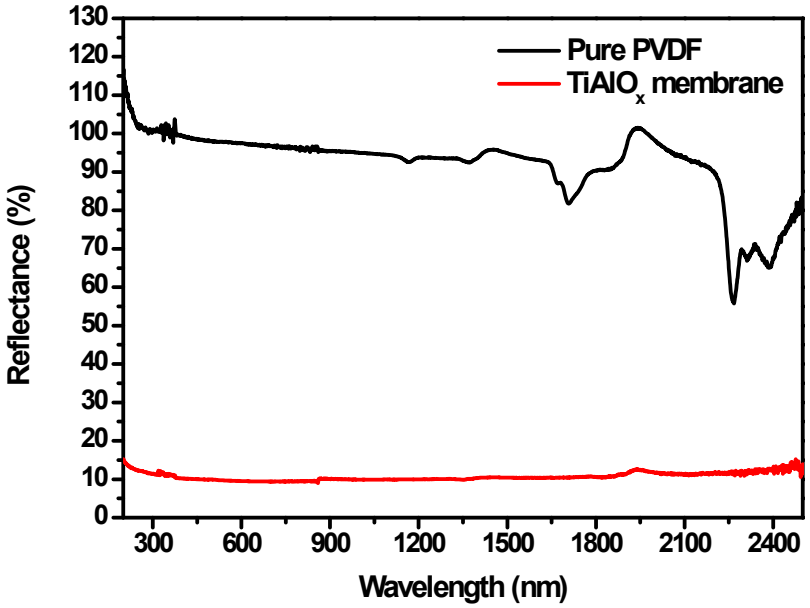

Figure S18. UV-Vis-NIR diffuse reflectance spectra of pure PVDF and TiAlOx membrane. The results show that the average optical absorption efficiency of pure PVDF is only 5.36%, even lower than that of $BaSO_4$ standard sample in the UV, which results in negative optical absorption of pure PVDF in the UV region. When $TiAlO_x$ powder was compounded with PVDF, $TiAlO_x$ photothermal membrane maintained the optical absorption performance of $TiAlO_x$ powder, and the average optical absorption efficiency was still reached 89.70%. It shows that PVDF can support $TiAlO_x$ powder well, and has no obvious influence on the optical absorption properties of $TiAlO_x$ powder. It can be seen that PVDF is an ideal supporting material for photothermal materials, and PVDF and $TiAlO_x$ powder are an ideal combination.

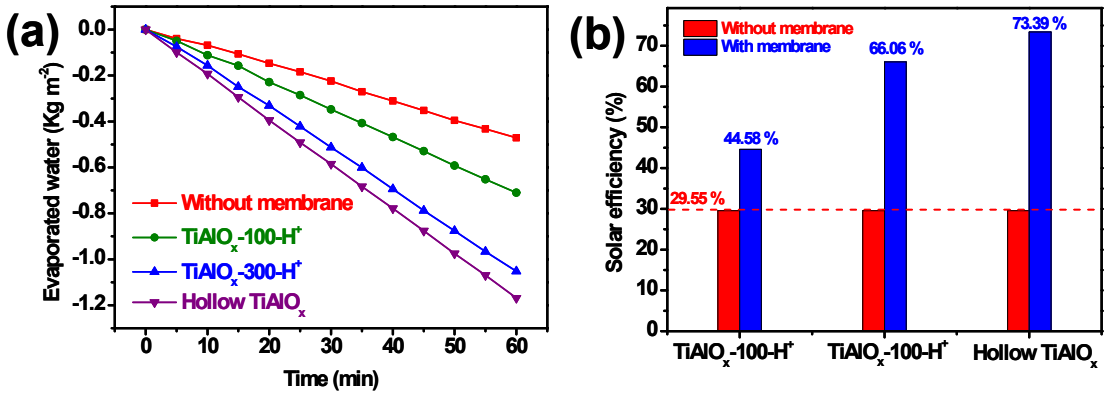

Figure S19. (a) Evaporation water weights against time with and without hollow $TiAlO_x$ membrane in different water and (b) corresponding solar efficiency.

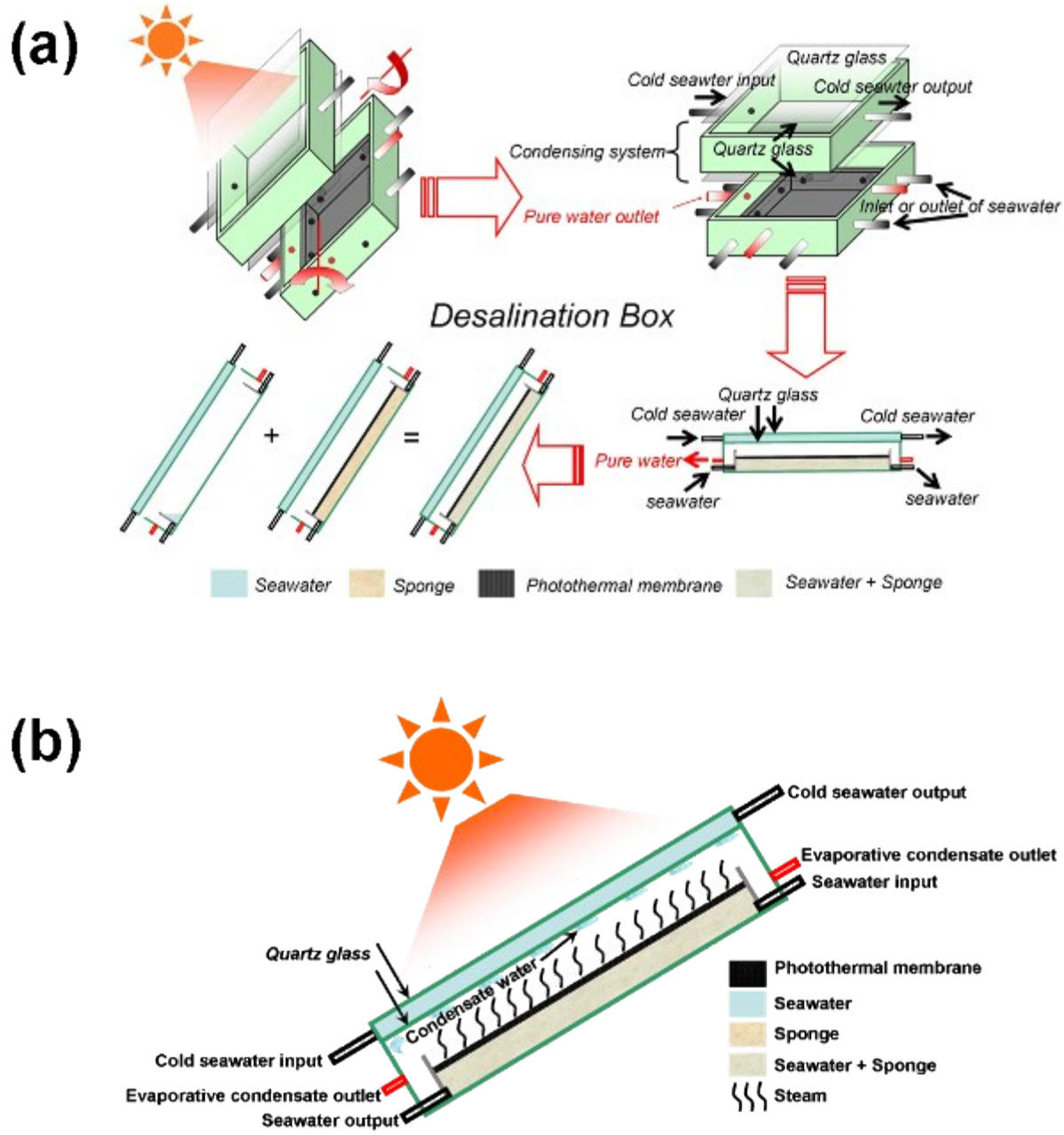

Figure S20. (a) Schematic of the desalination box for automatic tracking solar desalination system. (b) Schematic of working principle of desalination box work. As can be seen from Figure S20b, the working principle of the desalination box can be summarized as follows: first, the sponge is covered with seawater, and the seawater flows freely in the sponge. Secondly, the photothermal membrane produces photothermal effect under the sunlight, evaporating the seawater to form water vapor. Finally, when the vapor rises, it encounters a cold quartz glass that condenses into droplets, which accumulate slowly and grow from small to large. Then, the vapor flows along the quartz glass into the tank and flows into the pure water collection device. Under laboratory conditions, the device area is small and all parameters of desalination system can be accurately controlled, showing high efficiency. The

photothermal desalination system designed in this paper has two main processes, which reduce the overall efficiency of the photothermal desalination system. On the one hand, the evaporated water vapor cannot condense to the condensation system 100%. From the point of steam occurrence to the point of condensation, the steam flow process will be accompanied by heat loss, thus the steam temperature at the point of condensation will be lower than the steam temperature at the point of occurrence, resulting in a smaller thermal gradient, and a part of the water vapor cannot condense and return to the seawater. On the other hand, the condensation system of the photothermal desalination system described in this paper exchanges heat through circulating cold seawater, which reduces the thermal gradient between water vapor and condenser. Large area of circulating seawater is difficult to guarantee the fastest heat exchange, which also leads to the decrease of the thermal gradient between water vapor and condenser, which reduces the efficiency of the desalination system. Large-scale application will greatly enhance the above factors on the efficiency of photothermal desalination devices, so there is a big difference between laboratory scale and large-scale application.

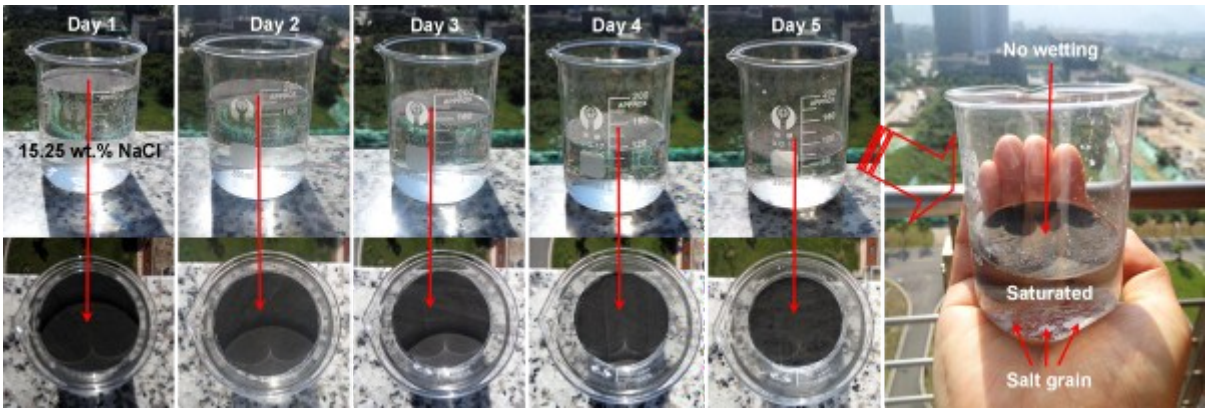

Figure S21. Digital photographics of $TiAlO_x$ photothermal membrane running for 5 days under natural light conditions. The photothermal membrane with a diameter of about 5.8 cm was put on 200 ml aqueous solution containing 200 ml 15% NaCl solution. The desalination experiment was carried out under natural light for 5 days without adding NaCl solution. As can be seen from Figure S21, after running for 5 days, the photothermal membrane can still self-float on the water surface without wetting. With the passage of time, the desalination efficiency of $TiAlO_x$ photothermal membrane remained relatively stable. At the same time, it should be pointed out that on the fifth day, a large number of salt grain were precipitated at the bottom of the beaker due to the continuous evaporation of water in the brine. However, no salt crystals were found at the top of the $TiAlO_x$ photothermal membrane. It can be seen that the $TiAlO_x$ photothermal membrane has no obvious solid salt accumulation during the long-term thermal desalination process, and shows good stability.

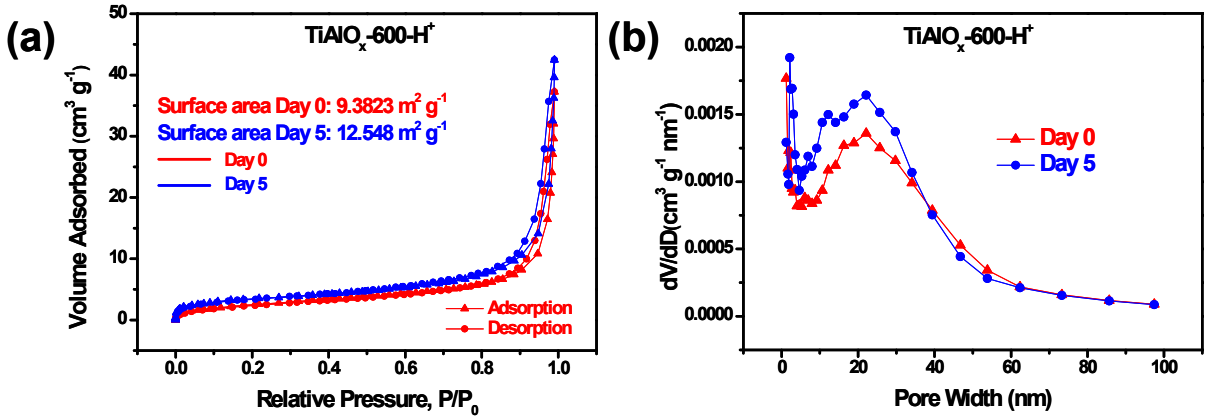

Figure S22. N_2 adsorption-desorption isotherm for the hollow black $TiAlO_x$ membrane after desalination for (a) 0 day and (b) 5 days. As can be seen from Figure S22, the BET surface area of the photothermal membrane only show slight change from 9.38 to 12.54 m^2 g^{-1} after 5-days operation, indicating that photothermal membrane can run stably in salt solution.

4. The calculation of light energy to heat of water evaporation efficiency (η)

The light energy to heat of water evaporation conversion efficiency (η) of the PVDF membranes containing with samples can be estimated by equation S2:[2]

$$\eta = \frac{Q_e}{Q_s} \qquad \text{S2}$$

where Q_s is the irradiation light power (1000 W m^{-2}), and Q_e is the power for evaporation of the water, which can be estimated by equation S3:

$$Q_e = \frac{dm \bullet H_e}{dt} = v \bullet H_e \qquad \text{S3}$$

where m is the mass of evaporated water, t is the time, v is the evaporation rate of water, H_e is the heat of evaporation of water (≈ 2260 kJ kg^{-1}),

$$m = \Delta m - \frac{\Delta m_{water} \cdot (S_{water} - S)}{S_{water}} \qquad \text{S4}$$

m indicates that the weight change of the evaporation device caused by the photothermal effect of membrane, Δm is the weight change of evaporation device, Δm_{water} is the weight change of evaporation device by without membrane, S_{water} is the water surface area, S is the membrane area. The water evaporation rate (v) was calculated by linear fitting. The power to evaporate the water (Q_e) and the conversion efficiency (η) of the PVDF membrane contained with TiO_2, $TiAlO_x$-y-H^+, and $TiAlO_x$-y-H^+ were then calculated to be presented in Table S2.

Table S4. Comparison of the water evaporation rates and conversion efficiency with TiO_2, $TiAlO_x$-y-H^+, $TiAlO_x$-y-H^+, and without PVDF membrane.

Name	Evaporated object	Fitting equation	Evaporation rate of water [v, kg m^{-2} h^{-1}]	Power of evaporation of the water [Q_e, kJ m^{-2} h^{-1}]	Coversion efficiency [η, %]
water	H_2O	y = -0.0079x + 0.0081	0.4707	1063.88	29.55
PVDF		y = -0.011x - 0.0006	0.6562	1482.99	41.19
TiO_2		y = -0.0102x - 0.0017	0.6191	1399.07	38.86
$TiAlO_x$-100-H^+		y = -0.012x + 0.0109	0.7101	1604.89	44.58
$TiAlO_x$-300-H^+		y = -0.0177x + 0.0161	1.0523	2378.22	66.06
$TiAlO_x$-600-H^+		y = -0.0194x - 0.0017	1.169	2642.01	73.39
$TiAlO_x$-600-H^+	Artificial seawater	y = -0.0197x + 0.0185	1.1692	2642.39	73.40
	8.26 wt.% NaCl	y = -0.0196x + 0.0193	1.1667	2636.74	73.24
	15.25 wt.% NaCl	y = -0.0190x + 0.0115	1.1318	2557.87	71.05
	26.47 wt.% NaCl	y = -0.0146x - 0.0015	0.8774	1982.92	55.08
Q_s = 1000 W m^{-2} h^{-1} = 3600 kJ m^{-2} h^{-1}					

Table S5 Measured concentration of four primary ions, Ti^{4+} and Al^{3+} in an artificial seawater, 8.26 wt.% NaCl, 15.25 wt.% NaCl, and 26.47 wt.% NaCl before and after desalination.

Elements (mg L^{-1})	Na^+	K^+	Mg^{2+}	Ca^{2+}	Ti^{4+}	Al^{3+}
Artificial Seawater	11869.05	3134.28	4171.41	458.6	—	—
Desalination	—	–	—	0.38	—	—
8.26 % NaCl	37279.88	×	×	×	×	×
Desalination	—	×	×	×	×	×
15.25 % NaCl	73709.28	×	×	×	×	×
Desalination	—	×	×	×	×	×
26.47 % NaCl	124754.8	×	×	×	×	×
Desalination	—	×	×	×	×	×
ICP-OES detection limit	0.02	0.15	0.02	0.003	0.03	0.025

"×" : Not detected, "—" :blow the detection limit

5. Evaluating the cost of the hollow $TiAlO_x$ hybrid PVDF microporous membrane

Table S6. The price of reagents.

Reagents	Price	manufacturer
commercial TiO_2	48￥/100 g (0.71￥ / g)	Macklin Biochemical Co., Ltd
commercial Al	55￥/100 g (0.55￥ / g)	Energy chemical Company
PVDF	210￥/300 g (0.268￥ / g)	Arkema (HSV900, France)
DMF	19￥/500ml (0.038￥ / mL)	Sinopharm Chemical Reagent Co., Ltd

0.8 g $TiAlO_x$ hybrid + 0.1 g PVDF + 1mL DMF can be prepared for 77 cm^2 $TiAlO_x$ hybrid PVDF microporous membrane (Reclaim 1.4 g hollow $TiAlO_x$ with 2g TiO_2 + Al to calculate cost). Evaluating the cost of the $TiAlO_x$ hybrid PVDF membrane (77 cm^2):

$$0.71 \times 0.48 + 0.43 \times 0.55 + 0.7 \times 0.1 + 0.038 \times 1 \text{ ￥} = 0.685 \text{ ￥}.$$

Therefore, preparing 1 m^2 $TiAlO_x$ hybrid PVDF microporous membrane need:

$$0.685\text{￥} / 77\ cm^2 = 88.96\ \text{￥} / m^2 \approx \mathbf{13.44}\ \$ / m^2.$$

Considering that entire preparation process is quite simple, and only electricity will be consumed, the total cost could be very attractive compared with the noble metal and new carbon materials.

6. Comparison of the evaporation rate of the water in recently reports

Table S7. Comparison of the evaporation rate (under 1000 W m^{-2}) of the water in recently reports.

Sample	Evaporation rate of the water (v, kg m^{-2} h^{-1})	Conversion efficiency (η, %)	Dimensions of photothermal devices (cm or cm^2)	reference
Black TiOx	0.8012	50.30%	5 (diameter)	1
PPy coated SS	0.92	58%	~ 3.5 (diameter)	2
Au nanoparticle /AAM	1.02	64%	2.8 (diameter)	3
Black gold membrane	0.68	42.5%	~ 1.5 (diameter)	4
Carbon foam / Graphene	1.02	64%	5 (diameter)	5
RGO / MCE	~ 0.96	~ 60%	3.8 (diameter)	6
rGO-Fe_3O_4	1.12	70%	Powder	7
Carbon black in PVA	0.55	53.8%	3.3 × 6.8	8
Graphene	0.76	48%	3.75 (diameter)	9
Ti_2O_3	1.32	83%	2.1 × 2.1	10
HCuPO−PDMS sheet	1.13	63.6%	0.95 × 0.95	11
Cu_7S_4	1.228	77.1%	Powder	12
Black Titania Nanocage	1.13	70.9%	5 (diameter)	13
Al nanoparticle /AAM	~ 0.92	~ 58%	2.8 (diameter)	14
2D Ti_3C_2 MXene	1.31	71%	4 (diameter)	15
Hollow $TiAlO_x$ Membrane	**1.17**	**73.4%**	**100 × 100**	**This work**

7. $TiAlO_x$ powder photothermal performance test:

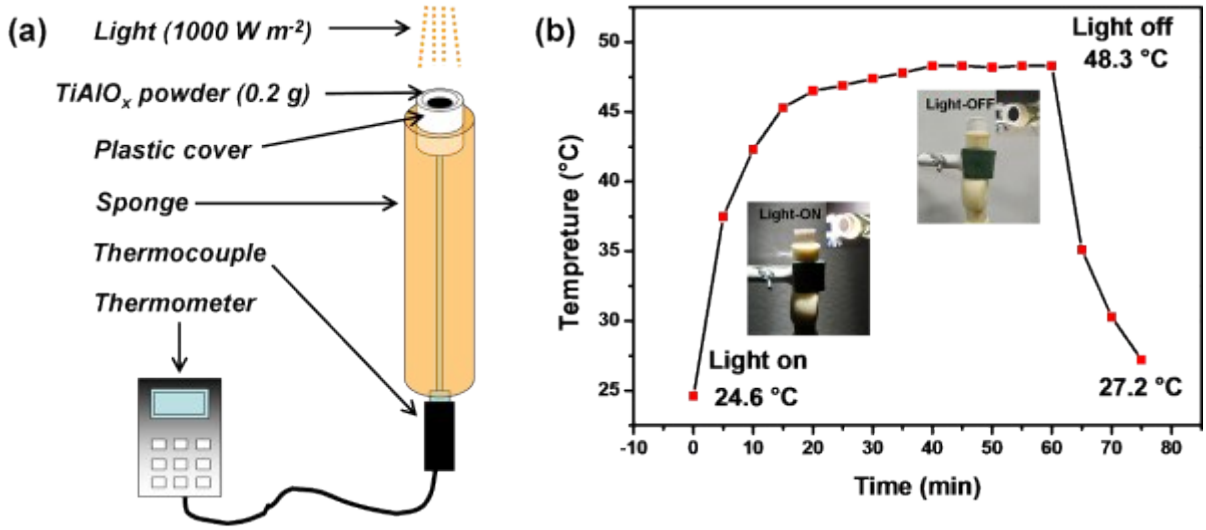

Figure S23. (a) Schematic of photothermal effect experiment. (b) Experimental results of photothermal effect.

8. Effect of photothermal membrane thickness on water evaporation efficiency

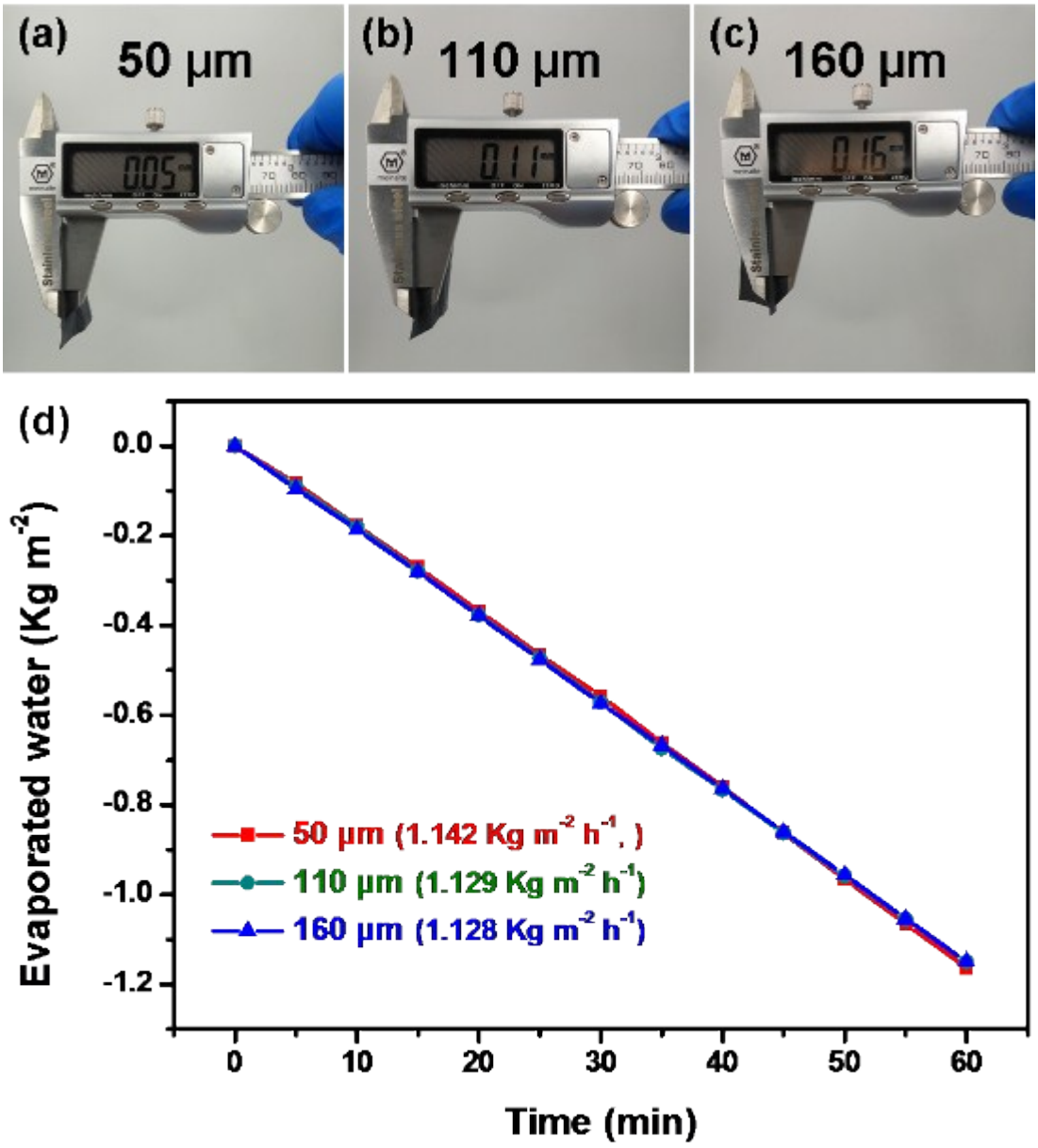

Figure S24. Different thickness of photothermal membrane (a) 50μm, (b) 110μm, (c) 160μm, and (d) corresponding evaporation efficiency. As can be seen from Figure S24, there is no significant change in water evaporation efficiency with the increase of membrane thickness within the membrane thickness range designed by us, indicating that the membrane thickness has no obvious effect on water evaporation efficiency within this thickness range. However, it should be pointed out that with the increase of membrane thickness, the photothermal evaporation efficiency of the membrane tends to decrease (Table S8).

Table S8. Evaporation rate of $TiAlO_x$ photothermal membrane with different thickness

Membrane thickness	**Evaporated object**	**Fitting equation**	**Evaporation rate of water [v, kg m^{-2} h^{-1}]**	**Power of evaporation of the water [Q_e, kJ m^{-2} h^{-1}]**	**Coversion efficiency [η, %]**
50 μm	H_2O	y = -0.0196x + 0.0179	1.1640	2630.88	73.07
110 μm		y = -0.0193x - 0.007	1.1505	2600.37	72.22
160 μm		y = -0.0192x - 0.0032	1.1496	2598.34	72.17
Q_s = 1000 W m^{-2} h^{-1} = 3600 kJ m^{-2} h^{-1}					

9. References

1 M. Ye, J. Jia, Z. Wu, C. Qian, R. Chen, P. G. O'Brien, W. Sun, Y. Dong, G. A. Ozin, *Adv. Energy Mater.,* 2016, **7**, 1601811..

2 L. Zhang, B. Tang, J. Wu, R. Li, P. Wang, *Adv. Mater.,* 2015, **27**, 4889-4894.

3 L. Zhou, Y. Tan, D. Ji, B. Zhu, P. Zhang, J. Xu, Q. Gan, Z. Yu, J. Zhu, *Sci. Adv.,* 2016, **2**, e1501227.

4 K. Bae, G. Kang, S. K. Cho, W. Park, K. Kim, W. J. Padilla, *Nat. Commun.,* 2015, **6**, 10103.

5 H. Ghasemi, G. Ni, A. M. Marconnet, J. Loomis, S. Yerci, N. Miljkovic, G. Chen, *Nat. Commun.,* 2014, **5**, 4449.

6 G. Wang, Y. Fu, X. Ma, W. Pi, D. Liu, X. Wang, *Carbon,* 2017, **114**, 117-124.

7 X. Wang, G. Ou, N. Wang, H. Wu, *ACS Appl. Mater. Inter.,* 2016, **8**, 9194-9199.

8 P. D. Dongare, A. Alabastri, S. Pedersen, K. R. Zodrow, N. J. Hogan, O. Neumann, J. Wu, T. Wang, A. Deshmukh, M. Elimelech, Q. Li, P. Nordlander, N. J. Halas, *Proc. Natl. Acad. Sci. U S A,* 2017, **114**, 6936-6941.

9 J. Yang, Y. Pang, W. Huang, S. K. Shaw, J. Schiffbauer, M. A. Pillers, X. Mu, S. Luo, T. Zhang, Y. Huang, G. Li, S. Ptasinska, M. Lieberman, T. Luo, *ACS Nano,* 2017, **11**, 5510-5518.

10 J. Wang, Y. Li, L. Deng, N. Wei, Y. Weng, S. Dong, D. Qi, J. Qiu, X. Chen, T. Wu, *Adv Mater.,* 2017, **29**, 1603730.

11 Z. Hua, B. Li, L. Li, X. Yin, K. Chen, W. Wang, *J. Phys. Chem. C,* 2016, **121**, 60-69.

12 C. Zhang, C. Yan, Z. Xue, W. Yu, Y. Xie, T. Wang, *Small,* 2016, **12**, 5320-5328.

13 G. Zhu, J. Xu, W. Zhao, F. Huang, *ACS Appl. Mater. Inter.,* 2016, **8**, 31716-31721.

14 L. Zhou, Y. Tan, J. Wang, W. Xu, Y. Yuan, W. Cai, S. Zhu, J. Zhu, *Nat. Photonics,* 2016, **10**, 393-398.

15 J. Zhao, Y. Yang, C. Yang, Y. Tian, Y. Han, J. Liu, X. Yin, W. Que, *J. Mater. Chem. A,* 2018, **6**, 16196-16204.